separations

MDPI

Article

Insights into the Adsorptive Separation of Ethylene/Ethane in LTA-Type Zeolites

Xiaohui Zhao [1], Shixue Zhou [2,*], Magdy Abdelghany Elsayed [1], Zhongyuan Chen [2], Chunhui Jiang [1], Yongli Hu [1] and Gumawa Windu Manggada [1]

[1] College of Energy and Mining Engineering, Shandong University of Science and Technology, Qingdao 266590, China; 18535824890@163.com (X.Z.); magdyabdelghany10@163.com (M.A.E.); 17853270569@163.com (C.J.); 13137448990@163.com (Y.H.); gumawawindu@gmail.com (G.W.M.)
[2] College of Chemical and Biological Engineering, Shandong University of Science and Technology, Qingdao 266590, China; chenzhongyuan299@163.com
* Correspondence: zhoushixue66@163.com

Abstract: Understanding the competitive adsorption mechanism is essential for the development of adsorptive separation of ethylene (C_2H_4) and ethane (C_2H_6). In this work, density functional theory calculations and molecular dynamics simulations were employed to investigate the adsorption of C_2H_4 and C_2H_6 in two LTA-type zeolites, ITQ-29 and 5A. The results show that the adsorption energies of the gas molecules in zeolite 5A are more negative than in ITQ-29, and the difference in adsorption energy between C_2H_4 and C_2H_6 in zeolite 5A is significantly larger than in ITQ-29, 13.3 versus 6.2 kJ/mol. Zeolite ITQ-29 demonstrates high C_2H_4/C_2H_6 ideal selectivity (43.5 at 5 ns) while exhibiting slow C_2H_4 uptake efficiency due to the small pore windows, hindering C_2H_4 diffusion (1.05×10^{-10} m^2/s at 298 K). In contrast, zeolite 5A facilitates the faster diffusion of C_2H_4 molecules (3.25×10^{-9} m^2/s at 298 K) and exhibits a modest C_2H_4/C_2H_6 selectivity of 1.11 at 5 ns in single-gas adsorption and 2.72 in equimolar binary mixture adsorption. To enhance C_2H_4/C_2H_6 selectivity, methyl phosphonic acid is introduced onto zeolite 5A to add a sieving layer that enables the C_2H_4 molecules to preferentially permeate, and the optimal coverage of methyl phosphonic acid is 50%, yielding a C_2H_4/C_2H_6 selectivity of 17.5 at 5 ns in mixture adsorption and preserving the C_2H_4 uptake efficiency. The insights into the competitive diffusion of molecules in the coating layer and inside the zeolites provide a theoretical basis for the rational design of high-performance adsorbents.

Keywords: adsorptive separation; LTA zeolite; surface modification; molecular dynamics simulation

check for updates

Academic Editor: Liming Zhang

Received: 22 April 2025
Revised: 22 May 2025
Accepted: 28 May 2025
Published: 1 June 2025

Citation: Zhao, X.; Zhou, S.; Elsayed, M.A.; Chen, Z.; Jiang, C.; Hu, Y.; Manggada, G.W. Insights into the Adsorptive Separation of Ethylene/Ethane in LTA-Type Zeolites. *Separations* **2025**, *12*, 146. https://doi.org/10.3390/separations12060146

Copyright: © 2025 by the authors. Licensee MDPI, Basel, Switzerland. This article is an open access article distributed under the terms and conditions of the Creative Commons Attribution (CC BY) license (https://creativecommons.org/licenses/by/4.0/).

1. Introduction

Light olefins are crucial feedstocks for the manufacture of plastics, rubber, and fibers [1,2]. In industry, the olefins are typically produced through catalytic cracking, steam cracking, and methanol conversion [3,4]. However, the resulting products contain alkanes that need to be separated to yield high-purity olefins for the synthesis of downstream products [5]. The separation of olefins and alkanes is one of the most technologically challenging and energy-intensive processes, with C_2H_4 and C_3H_6 separation from gas mixtures accounting for 0.3% of global energy consumption [6]. The cryogenic distillation process, commonly used in industry, necessitates the utilization of large-scale distillation columns of 120–180 trays, high pressures of 1.5–3 MPa, and sub-ambient temperatures of 123–263 K [7].

In contrast, the adsorptive separation process offers significant advantages of minimal energy consumption, high separation efficiency, and straightforward operation [8,9]. With the development of porous materials, such as zeolites [10,11], activated carbon [12,13], metal-organic frameworks [14,15], covalent organic frameworks [16,17], and hydrogen-bonded organic frameworks [18,19], adsorptive separation has become increasingly attractive [20].

The design of porous materials possessing high adsorption selectivity remains a significant challenge in the field of separation of olefins and alkanes with similar molecular sizes and physicochemical properties, which prompts extensive experimental and theoretical studies. Zeolites are widely used in adsorptive separation due to their favorable characteristics, such as well-defined pores, large specific surface area, high chemical and thermal stability, and low cost [21–23]. Moreover, the adsorption selectivity in zeolites can be improved by adjusting frameworks, tuning pore structures, varying exchangeable cations, and modifying surfaces. LTA-type zeolite frameworks feature 8-membered ring windows connecting supercages [24], exhibiting a favorable sieving effect for molecules with kinetic diameters in the range of 3.9–4.3 Å [25,26]. Rege et al. [27] employed zeolite 4A for the separation of C_3H_6 and C_3H_8 and found that C_3H_8 is sterically excluded from the pores, whereas C_3H_6 can readily diffuse through the zeolite, attributing this to the effective pore aperture being the demarcation between the kinetic diameters of C_3H_6 and C_3H_8 molecules. Sala et al. [28] synthesized a novel zeolite, designated ITQ-69, with a distinctive tri-directional pore-channel system that is particularly suitable for the kinetic separation of C_3H_6 and C_3H_8, and the experimental results demonstrate that the diffusion rate of C_3H_6 in the zeolite is significantly faster than that of C_3H_8. Chen et al. [29] reported that the framework Si/Al ratio of MOR-type zeolite regulates the number and distribution of exchangeable cations in the channels, thereby controlling the accessibility of guest molecules and the utilization of space, and an appropriate number of exchangeable cations can enhance the interaction between C_2H_4 and the zeolite, making the C_2H_4 molecules more readily access and utilize the space than C_2H_6. Baamran et al. [30] found that doping ferric oxide nanoparticles into zeolite 13X augments the adsorption capacity by surface electron transfer, which strengthens π–ion interactions between C_2H_4 molecules and adsorption sites. Additionally, the introduction of ferric oxide results in the formation of nanochannels, thereby enhancing the sieving effect and improving C_2H_4 selectivity. Ellis et al. [31] demonstrated that surface coating with phosphonic acids of varying alkyl tail length on zeolite 5A enhances the separation of C_3H_6 and C_3H_8 through restricting the C_3H_8 adsorption rate. Zhou et al. [32] found that C_3H_6/C_3H_8 kinetic selectivity is improved by increasing phosphonic acids coating density on zeolite 5A and employing phosphonic acids with terminal functional group (amine or carboxylic acid).

Furthermore, with the development of science and technology, molecular simulation has been applied to study adsorptive separation [33]. Mitra et al. [34] simulated the diffusion behavior of C_3H_6 in zeolites ZSM-5 and Na-Y and found that the molecular diffusion is strongly dependent on pore structure, where zeolite ZSM-5, featuring a network of intersecting channels, restricts the translational diffusion of C_3H_6 molecules and causes the molecules to orientate along the channels of the zeolite, whereas zeolite Na-Y, having spherical supercages interconnected through windows, enables C_3H_6 molecules to undergo isotropic rotation freely. Guo et al. [35] simulated the adsorptive separation of N_2 and O_2 in zeolite Li-LSX incorporated with Ag^+ and Ce^{3+} cations, and they found that Ag^+ doping enhances the adsorption of both N_2 and O_2, whereas Ce^{3+} doping only increases O_2 adsorption. Liu et al. [36] simulated the adsorption of Xe and Kr molecules in CHA-type zeolite with framework Si/Al ratio of 2.5 and Ca^{2+} as the counter-cations, and they found that the Ca^{2+} cations act as the primary binding sites for Xe molecules, whereas

Kr molecules are stabilized through weak adsorbent–adsorbate interactions with the zeolite framework.

In this work, the adsorption of C_2H_4 and C_2H_6 in two LTA-type zeolites, ITQ-29 and 5A, was investigated using first principle calculations based on density functional theory (DFT) and molecular dynamics (MD) simulations based on the molecular force field. The atomic charges, adsorbate structures, and adsorption energies were determined. The adsorption isotherms, molecular diffusion dynamics, and adsorption kinetics were simulated. To improve C_2H_4/C_2H_6 adsorption selectivity, methyl phosphonic acid (MPA) was introduced onto the surface of zeolite 5A. A diffusion-mediated competitive adsorption mechanism was demonstrated for the separation of C_2H_4 and C_2H_6 in zeolites, providing a new perspective on the separation of olefins and alkanes.

2. Materials and Methods

2.1. Structural Models and Density Functional Theory Calculations

Two LTA-type zeolites, ITQ-29 and 5A, were used for the adsorption of C_2H_4 and C_2H_6 in this work. The cell model of the zeolite ITQ-29 was built using the atomic coordinates in the literature [37], and the zeolite 5A was built using the atomic coordinates in the literature [38]. Then, the geometries were optimized using the DMol^3 module in the Materials Studio 2017 software (Accelrys Software Inc., San Diego, United States) based on DFT calculations. In the calculations, the Perdew–Burke–Ernzerhof (PBE) functional of the generalized gradient approximation (GGA) was adopted to evaluate the nonlocal exchange correlation energy [39]. The electron wave function was based on double numerical plus polarization (DNP) basis set to ensure the calculation accuracy [40], with basis file version 4.4. The self-consistent field tolerance was set at 10^{-6} Ha. To accelerate the self-consistent field convergence, the direct inversion in an iterative subspace (DIIS), preconditioner, and smearing were enabled, with parameters set at 6, 4.0 ${a_0}^{-1}$, and 0.005 Ha, respectively. Hexadecapole was chosen for multipolar expansion to describe the electron distribution. The global orbital cutoff scheme was applied with a cutoff distance of 4.8 Å. Gamma point only is used for sampling in the first Brillouin zone, since the system is large enough that the electronic wavefunctions are sufficiently smooth in real space. For geometry optimization, the convergence criteria of the energy, maximum force, and maximum displacement were set at 1.0×10^{-5} Ha, 0.002 Ha Å^{-1}, and 0.005 Å, respectively.

The ITQ-29 and 5A structural models after geometry optimization are shown in Figure 1(A1) and Figure 1(B1), respectively, in which the zeolites consist of three distinct building units: double-4-membered ring (D4R), sodalite cage (β cage), and LTA supercage (α cage). The framework is composed of β cages arranged in simple cubic packing, with adjacent β cages connected by D4R units, and eight β cages surrounding a central α cage. In zeolite 5A, the Na^+ and Ca^{2+} cations are located near the centers of the 6-membered rings of the α cages, as shown in Figure S1. The geometry optimization did not alter the atomic coordinates or cell parameters compared with those in the literature [37,38], as listed in Tables S1 and S2, confirming that the DFT calculation parameters are reliable.

The X-ray diffraction patterns of the cell models were simulated using the powder diffraction task of the Reflex module in the Materials Studio software. To generate the X-ray diffraction patterns, incident radiation of average wavelength 1.541838 Å (Cu K_α radiation) was employed over diffraction angle (2θ) from 5 to 50° at a step size of 0.02°. The peak profile was described using Pseudo-Voigt function with profile parameters N_A and N_B set at 0.5 and 0.0, and the U, V, and W parameters to calculate instrumental broadening of the peaks were set at 0.02, −0.01, and 0.02°[2], respectively. The simulated X-ray diffraction patterns, as shown in Figure 1(A2,B2), are similar to those observed in the experimental measurements [37,41], indicating that the cell models are reliable.

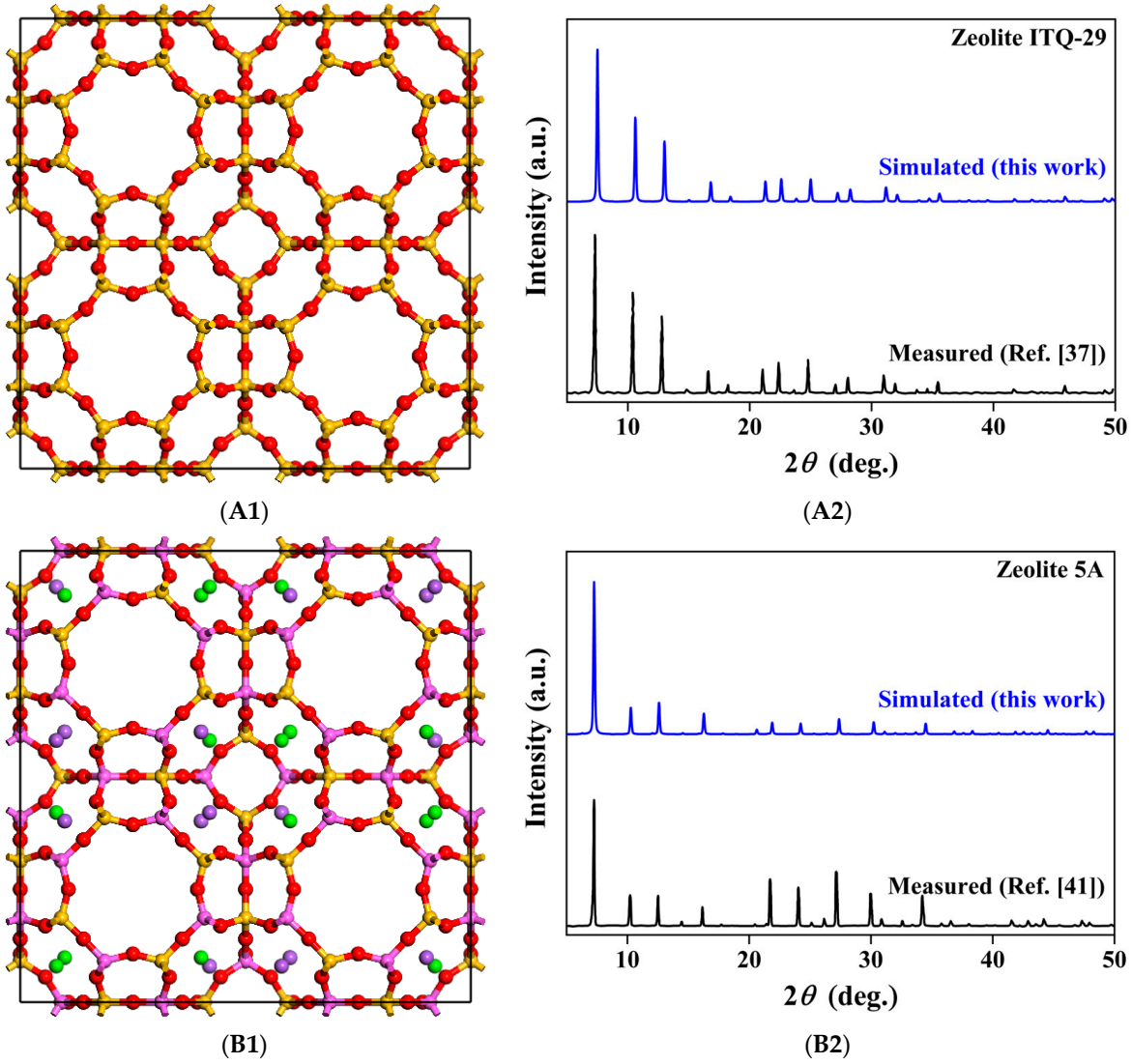


Figure 1. Structural models and X-ray diffraction patterns of the zeolites ITQ-29 (**A1**,**A2**) and 5A (**B1**,**B2**). Spheres: yellow (Si), red (O), pink (Al), purple (Na), and green (Ca). The lattice parameters for zeolite ITQ-29 are $a = b = c = 23.70$ Å, and for zeolite 5A, $a = b = c = 24.84$ Å. The chemical formula of the structural model for zeolite ITQ-29 is $Si_{192}O_{384}$, and that for zeolite 5A is $Ca_{32}Na_{32}Si_{96}Al_{96}O_{384}$.

The Hirshfeld population analysis was performed on the DFT-calculated electron densities to determine the atomic charges in the zeolites. The atomic charges are crucial for the simulation accuracy, which govern the electrostatic interactions between adsorbent and adsorbate, thereby affecting the molecular loading in grand canonical Monte Carlo (GCMC) simulations and the molecular diffusion trajectories in molecular dynamics simulations. The average Hirshfeld atomic charges in the zeolites ITQ-29 and 5A are listed in Table S3, which are close to those in the literature [42]. When the Hirshfeld charges were used for adsorption simulation with COMPASSII force field, the resulting isotherm is closer to those experimentally measured [43] than those simulated using Mulliken, ESP, QEq, or Gasteiger charges, as shown in Figure S2 and Table S4.

The geometries of the ITQ-29 and 5A cells with an adsorbed C_2H_4 or C_2H_6 molecule near a 6-membered ring were optimized based on DFT calculations. Then, the adsorption energy of the molecule was calculated by subtracting the individual energies of the zeolite and molecule from the total energy of the system.

The supercell surface models of the zeolites used for molecular dynamics simulations were constructed based on the cell models (Figure 1(A1,B1)). First, a p(1 × 1) slab with

a thickness of two cells was created through cleaving the cell along the (0 0 1) plane, specifying slab thickness to 2.0 cells, slightly increasing the slab thickness to ensure that the bottom face was terminated only with O atoms, adjusting the distance from the origin to the top face to achieve O atoms only termination, and capping the dangling O atoms at the top and bottom faces with H atoms to maintain chemical stability. Next, a vacuum layer of 500 Å was added above the slab to avoid interactions between periodic images and to serve as a gas reservoir. Finally, geometry optimization based on DFT calculations was performed. The supercell surface model for zeolite ITQ-29 is shown in Figure S3, and that for zeolite 5A is shown in Figure S4. The atomic charges in the supercell surface models were determined through Hirshfeld population analysis.

For zeolite 5A with MPA, the MPA molecules were anchored on the top face of the slab via P-O-Si/Al bonds. After geometry optimization, the fully (100% coverage) MPA-coated supercell surface model is shown in Figure S5. For 25%, 50%, 75%, and 100% coverages of MPA, each pore window has 1, 2, 3, and 4 acid molecules, respectively, as shown in Figure S6.

2.2. Grand Canonical Monte Carlo Simulations

The adsorption isotherms of C_2H_4 and C_2H_6 in the ITQ-29 and 5A cells were simulated using the Sorption module in the Materials Studio software with GCMC method based on the molecular force field. The COMPASSII force field was selected for the simulation, which yielded isotherms closer to the experimentally measured (in loading amount and curve shape) ones that are reported in reference [43] than those obtained using the Dreiding, Universal, CVFF or PCFF force fields, as shown in Figure S7. For van der Waals interactions, the atom-based method was used for summation, cubic spline was used for energy truncation, a spline width of 1 Å was used for the truncation, and the cutoff distance was set at 12 Å, which is sufficiently long (validated by testing, as shown in Figure S8) yet remains less than half of the cell edge length to avoid spurious self-interactions. For electrostatic interactions, the Ewald method was used for summation. The Hirshfeld atomic charges derived from DFT calculations for the molecules and zeolites (the average Hirshfeld atomic charges are listed in Tables S3 and S5) were used for the simulation instead of the formal charges in the force field files. The equilibration steps and production steps were both set at 1×10^6, a value sufficiently large to balance computational accuracy and efficiency (validated by testing, as shown in Figures S9 and S10). The β cages of the zeolites were blocked using He atoms in the simulation to prevent unphysical occupation by C_2H_4 and C_2H_6 molecules. If using a CVFF forcefield for GCMC simulations, the C_2H_4 loadings at low pressures or high temperatures were overestimated, and the C_2H_6 loadings were always overestimated, compared with the experimentally measured data reported in reference [43], as shown in Figure S11.

2.3. Molecular Dynamics Simulations

The molecular dynamics simulations of C_2H_4 and C_2H_6 in ITQ-29 and 5A cells were performed using the Large-scale Atomic/Molecular Massively Parallel Simulator (LAMMPS) 2Aug2023 software (Sandia National Laboratories), which provided better computational efficiency than the Forcite module in the Materials Studio software for the large-scale simulation. In the simulations, the CVFF force field, rigorously validated for zeolite systems [44,45], was employed for simulating molecular diffusion in zeolites, and the Hirshfeld atomic charges derived from DFT calculations were used, by which molecular diffusion coefficients comparable to the experimentally measured that reported in reference [44] were derived. The units, atom_style, and time step were set at real, full, and 1 fs, respectively. The boundary was set at p p p. The comm_style was set at tiled,

and comm_modify was set at mode single cutoff 14.0. For intramolecular interactions, the bond, angle, and dihedral styles were all set at harmonic. The pair_style was set at lj/cut/coul/long 12.0 12.0, and pair_modify was set at shift yes mix arithmetic. The kspace_style was set at pppm 1.0×10^{-5}. The Nosé–Hoover thermostat was employed for the temperature control. After molecular dynamics simulations, the mean square displacement (MSD) versus time was plotted and linear fitting was performed, and then the diffusion coefficient was determined from the slope of the fitted line divided by 6 according to the Einstein relation.

The adsorption kinetics were extracted from the simulations performed on the supercell surface models to plot the time-dependent uptake profiles. The adsorption temperature was set at 298 K (a higher temperature is not favorable for gas uptake (Figure S12)). For single-gas adsorption, 100 molecules were put in the gas reservoir of the supercell surface model (the number of molecules is sufficient, otherwise an insufficient number of molecules results in inefficient uptake (Figure S13)). The simulation timescale was typically set at 5 ns to balance result visualization and computational efficiency (Figure S14). The supercell surface model with a suitable slab thickness of two cells was employed (Figure S15). The ideal selectivity was determined by the ratio of C_2H_4 to C_2H_6 uptakes at the same adsorption time in single-gas adsorption, and the mixture selectivity was determined by the uptake ratio of C_2H_4 to C_2H_6 in mixed-gas adsorption divided by their content ratio in the feed gas.

3. Results and Discussion

3.1. Adsorption Structures and Adsorption Energies

After geometry optimization based on DFT calculations, the adsorption structures of the C_2H_4 and C_2H_6 molecules in zeolites ITQ-29 and 5A are shown in Figure 2. In zeolite ITQ-29, the distances between the C atoms of the C_2H_4 molecule and the proximal O atoms in host 6-membered ring (3.79–3.87 Å) are shorter than the corresponding distance for the C_2H_6 molecule (4.36–4.47 Å). This originates from the difference in molecular geometry between C_2H_4 and C_2H_6. The C_2H_4 molecule exhibits a lower steric hindrance than C_2H_6 to access the 6-membered ring in zeolite ITQ-29. In zeolite 5A, the C_2H_4 molecule is much closer to the 6-membered ring with a distance of 3.55–3.76 Å, while the C_2H_6 molecule maintains a larger distance of 4.30–4.56 Å. This is attributed to the presence of Ca^{2+} cations in zeolite 5A, which exert strong attraction to the C_2H_4 molecule.

The adsorption energies of the C_2H_4 and C_2H_6 molecules in zeolites ITQ-29 and 5A are listed in Table 1 and Table S6. In zeolite ITQ-29, the adsorption energy of C_2H_4 is more negative than C_2H_6 (−27.7 vs. −21.5 kJ/mol), which is attributed to the stronger orbital hybridization of the C atoms of C_2H_4 with the O atoms in host 6-membered ring, as shown in Figure S16. In zeolite 5A, the adsorption energies of C_2H_4 and C_2H_6 are −45.6 and −32.3 kJ/mol, respectively, more negative than in zeolite ITQ-29. This enhanced adsorption results from stronger interactions between adsorbate molecules and zeolite 5A with exchangeable cations (Table S7), as evidenced by orbital hybridization (Figure S17) compared with those in zeolite ITQ-29 (Figure S16). Although the adsorption is enhanced for both C_2H_4 and C_2H_6 in zeolite 5A, the difference in adsorption energy between C_2H_4 and C_2H_6 in zeolite 5A is larger than that in ITQ-29, 13.3 vs. 6.2 kJ/mol, which is responsible for the competitive occupation of adsorption sites by C_2H_4 over C_2H_6 in zeolite 5A. The adsorption energies of C_2H_4 and C_2H_6 in zeolites ITQ-29 and 5A calculated in this work, without zero-point energy (ZPE) and vibration enthalpy calibration, are comparable to the experimentally measured adsorption enthalpies reported in references [46–48], indicating that physisorption dominates the adsorption behavior. The adsorption energies/enthalpies in zeolite 5A in this work and reference [48] are more negative than those in reference [47],

since the adsorption enthalpy is influenced by the relative amounts of Ca^{2+} and Na^{+} cations and when their amounts are similar, the adsorption enthalpy is more negative [48].

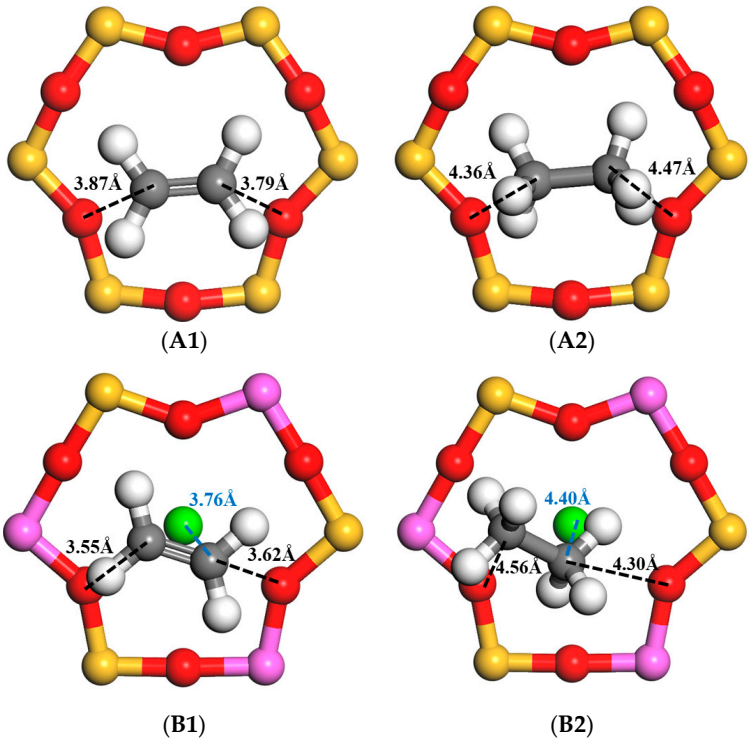


Figure 2. Adsorption structures of C_2H_4 and C_2H_6 molecules in zeolites ITQ-29 (**A1**,**A2**) and 5A (**B1**,**B2**). Spheres: yellow (Si), red (O), pink (Al), green (Ca), gray (C), and white (H). Only the 6-membered rings near the adsorbate molecules in the zeolite cells are shown in the figure, and the distances between each C atom of the molecules and its proximal O atom in host 6-membered ring of zeolite ITQ-29 or 5A and the minimal distances between C and Ca atoms in zeolite 5A are shown.

Table 1. Adsorption energies/enthalpies of C_2H_4 and C_2H_6 in zeolites ITQ-29 and 5A.

Adsorbent	Adsorbate	Adsorption Energy/Enthalpy (kJ/mol)	Source
ITQ-29	C_2H_4	−27.7	This work
ITQ-29	C_2H_6	−21.5	This work
5A	C_2H_4	−45.6	This work
5A	C_2H_6	−32.3	This work
ITQ-29	C_2H_4	−25.7	[46]
ITQ-29	C_2H_6	−23.0	[46]
5A	C_2H_4	−33.5	[47]
5A	C_2H_6	−27.6	[47]
5A	C_2H_4	−59.0	[48]
5A	C_2H_6	−37.0	[48]

3.2. Adsorption Isotherms

The single-component isotherms of C_2H_4 and C_2H_6 adsorption in zeolites ITQ-29 and 5A at different temperatures are shown in Figure 3 and the Langmuir model [49] provides excellent agreement with the adsorption data (Table S8, adj.$-R^2 > 0.999$). As the temperature increases, both loadings of C_2H_4 and C_2H_6 in the zeolites decrease sharply, and the loading differences between C_2H_4 and C_2H_6 also decrease, which indicates that a low temperature is favorable for the adsorptive separation of C_2H_4 and C_2H_6. As pressure increases, both loadings of C_2H_4 and C_2H_6 in the zeolites increase rapidly at low pressures owing to abundant adsorption sites, while the loadings approach asymptote at high pressures due to the progressive saturation of adsorption sites. Moreover, the loadings

in zeolite 5A are higher than in zeolite ITQ-29. This difference is attributed to their distinct chemical compositions. Zeolite 5A contains Ca^{2+} and Na^{+} cations, which enhance the adsorbent–adsorbate interactions through intensifying electrostatic interactions. In contrast, pure silica zeolite ITQ-29 lacks such cations, leading to weaker interactions dominated by van der Waals forces. This indicates that the exchangeable cations play a pivotal role in enhancing adsorption loadings in the zeolite.

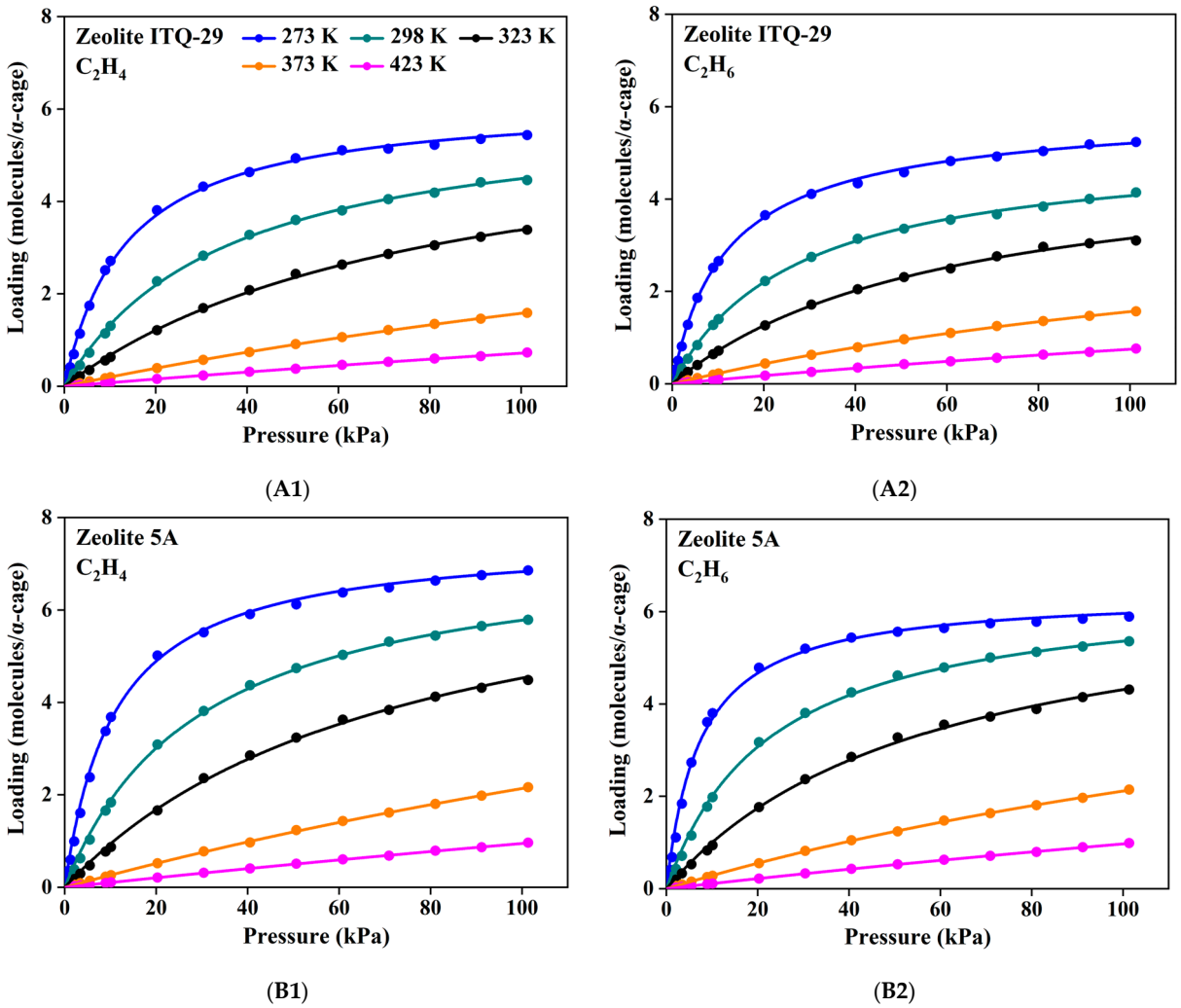


Figure 3. Adsorption isotherms of C_2H_4 and C_2H_6 in zeolites ITQ-29 (**A1**,**A2**) and 5A (**B1**,**B2**) at different temperatures. The data points are from GCMC simulations, and the solid lines represents the fittings of the data using the Langmuir model.

The adsorption isotherm for the mixture is affected by the ratio of C_2H_4 to C_2H_6, as shown in Figures S18 and S19. The C_2H_4 loading increases when the C_2H_4 proportion rises in the mixture. Both loadings of C_2H_4 and C_2H_6 are higher in zeolite 5A than in ITQ-29 due to the stronger interactions of gas molecules with zeolite 5A.

The energy distribution profiles for C_2H_4 and C_2H_6 adsorption in zeolites ITQ-29 and 5A at different temperatures are shown in Figure 4. The energy distribution exhibits the characteristics of single-site-dominated adsorption. As temperature increases, the curves shift to less negative energies, reflecting the weakening of the adsorption strength. This trend is consistent with the observed temperature-dependent adsorption isotherms, where a low temperature is favorable for gas adsorption. Moreover, the energies are more negative in zeolite 5A than in ITQ-29, as shown in Figure S20, which is attributed to the presence

of Ca^{2+} and Na^{+} cations in zeolite 5A, enhancing interactions with the molecules through molecular polarization and subsequent electrostatic reinforcement.

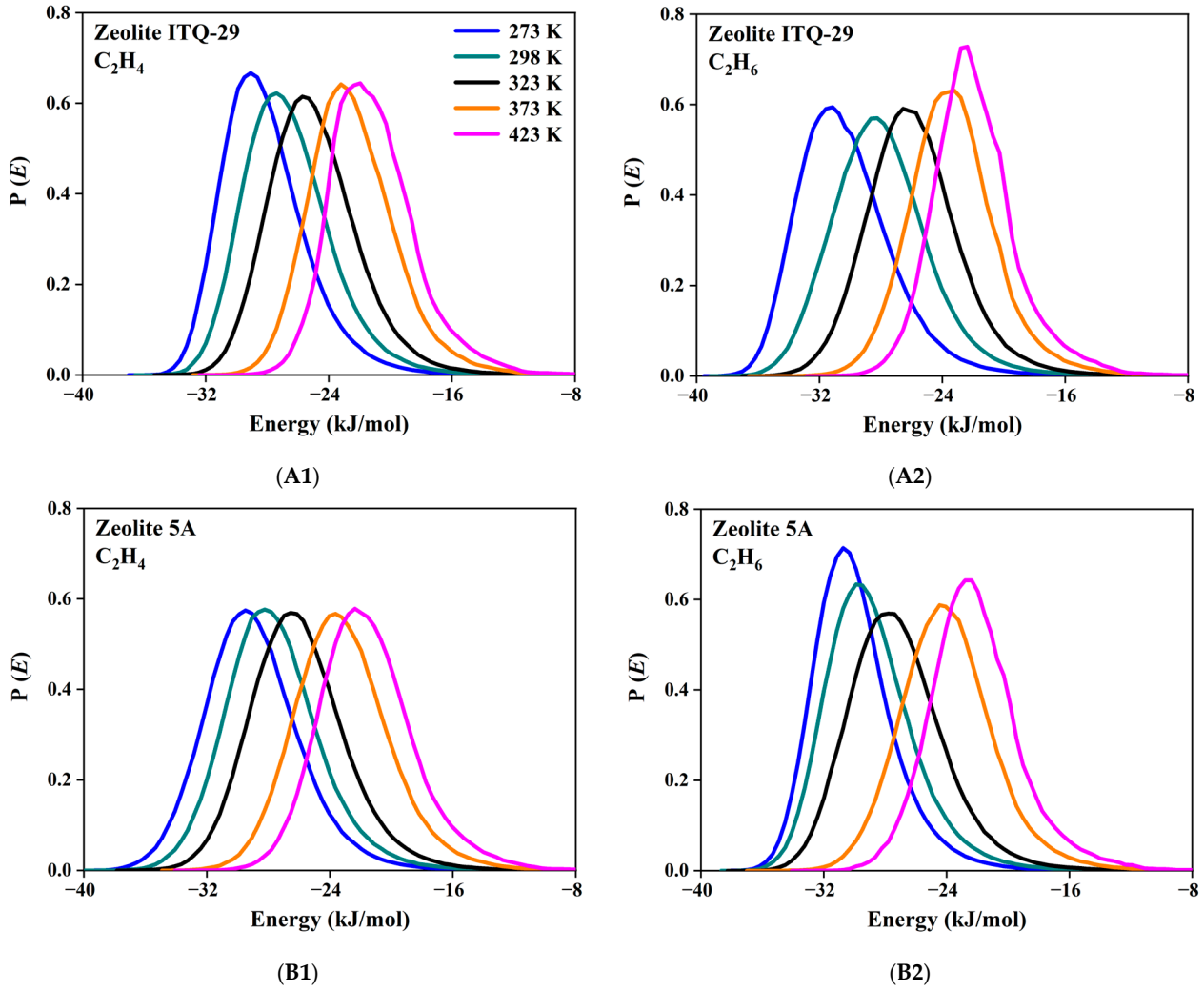


Figure 4. Energy distribution profiles for C_2H_4 and C_2H_6 adsorption in zeolites ITQ-29 (**A1**,**A2**) and 5A (**B1**,**B2**) under 101 kPa at different temperatures. The *y*-axis represents the probability density, P (*E*) (a.u.), which is normalized to unity. More negative energies represent stronger adsorbent–adsorbate interactions.

3.3. Diffusion Coefficients and Activation Energies

The diffusion coefficient is affected by the molecular loading in zeolite, as shown in Figure S21. With the increase in loading from 0.5 to 2.0 molecules/α-cage in zeolite 5A, the diffusion coefficient significantly decreases, and with a further increase in the loading, the coefficient almost remains constant. Therefore, simulations with 2.0 molecules/α-cage were performed for the further study of molecular diffusion in this section. The diffusion coefficients of C_2H_4 in zeolite 5A at different temperatures derived from the simulations using the LAMMPS software with CVFF forcefield are similar to the coefficients from the simulations using the Forcite module in the Materials Studio software (COMPASSII and CVFF forcefields), as listed in Table S9. The diffusion coefficients of C_2H_4 are higher than C_2H_6 at the same temperatures in both zeolites, as shown in Table S10, which is attributed to the smaller molecular size of C_2H_4 (minimum cross-section 3.30 × 4.20 Å) than C_2H_6 (minimum cross-section 3.90 × 4.18 Å) [50]. In zeolite 5A, both diffusion coefficients of C_2H_4 and C_2H_6 are much higher than in zeolite ITQ-29 at the same temperatures, which is ascribed to the larger 8-membered ring windows of α-cages in zeolite 5A than in ITQ-29

(4.21 vs. 4.15 Å [51]). As the temperature increases, the diffusion coefficients for C_2H_4 and C_2H_6 in zeolites ITQ-29 and 5A all increase.

The Arrhenius plots of the natural logarithm of the diffusion coefficients (ln *D*) versus inverse temperature ($1/T$) for C_2H_4 and C_2H_6 in zeolites ITQ-29 and 5A are shown in Figure 5. The activation energy of C_2H_4 diffusion is smaller than that of C_2H_6 in both zeolites, indicating that C_2H_4 diffusion is less temperature sensitive. In zeolite 5A, both activation energies of C_2H_4 and C_2H_6 are smaller than in zeolite ITQ-29. Moreover, the activation energy presents an inverse relationship with the diffusion coefficient. C_2H_4 exhibits smaller diffusion activation energy than C_2H_6 in both zeolites and higher diffusion coefficient in zeolite 5A than in ITQ-29, suggesting that zeolite 5A is a better adsorbent than ITQ-29 for the adsorptive separation of C_2H_4 over C_2H_6 at a lower temperature.

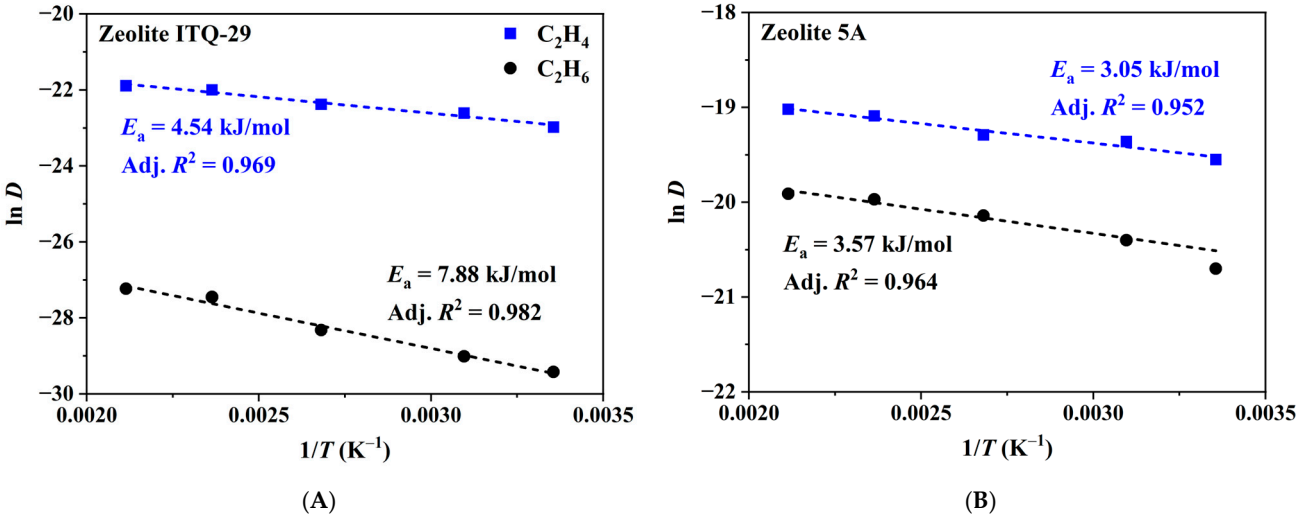


Figure 5. Arrhenius plots of ln *D* versus $1/T$ for C_2H_4 and C_2H_6 in zeolites ITQ-29 (**A**) and 5A (**B**). The data points are derived from simulations, and the dashed line represents the linear fit of the data. The linear fittings yield high adj.$-R^2$ values, indicating a strong correlation between the ln *D* and $1/T$. The activation energy E_a equals the slope of the fitted line multiplied by the negative value of the universal gas constant.

3.4. Adsorption Kinetics

In single-gas adsorption, the uptakes of C_2H_4 and C_2H_6 in zeolites ITQ-29 and 5A are shown in Figure 6, based on the simulation of gas molecules diffusing from the gas reservoir into the solid slab of the supercell surface models. In zeolite ITQ-29, the C_2H_4 uptake increases rapidly until 2 ns, followed by a slow increase due to the depletion of C_2H_4 molecules in the gas reservoir. Interestingly, the C_2H_6 uptake remains negligible throughout the simulation, indicating that C_2H_6 molecules are sterically excluded by the small pore windows of zeolite ITQ-29. In zeolite 5A, the C_2H_4 uptake increases sharply within 1 ns and achieves equilibrium at 2 ns, while C_2H_6 uptake increases slowly and achieves equilibrium at 3 ns. At 5 ns, the C_2H_4 uptake is higher than C_2H_6 in zeolite 5A (98 vs. 88 molecules per supercell), which is consistent with the adsorption isotherm analysis (Figure 3). In both zeolites, the uptake of C_2H_4 is faster than C_2H_6 and zeolite 5A exhibits faster adsorption for both gases than ITQ-29, which is attributed to the smaller molecular size of C_2H_4 than C_2H_6 and the larger pore window size of zeolite 5A than ITQ-29; it aligns with the diffusion coefficient trends (Table S10).

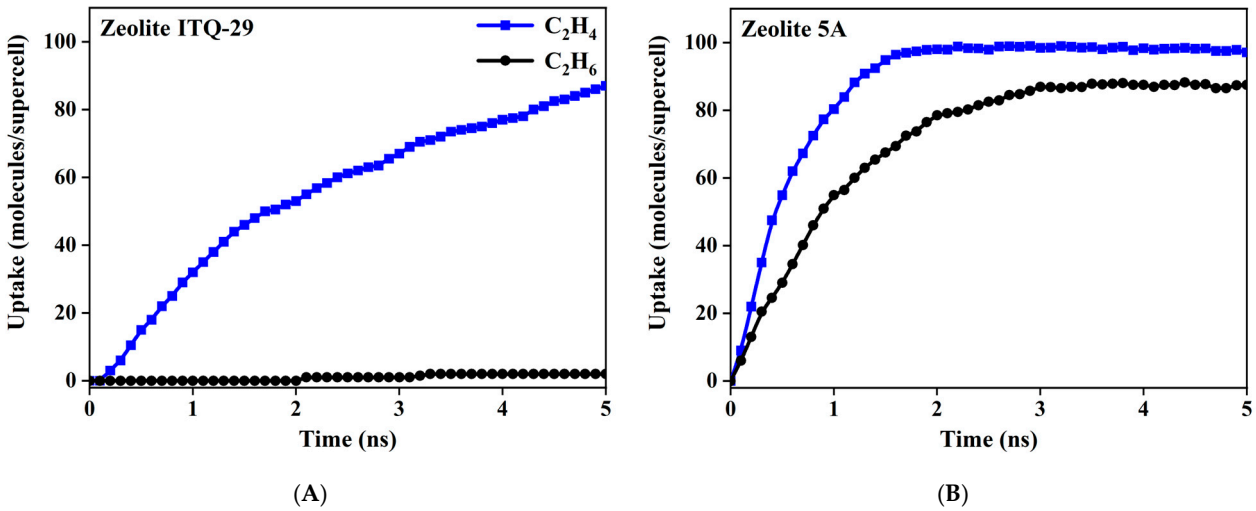


Figure 6. Uptakes of C_2H_4 and C_2H_6 in zeolites ITQ-29 (**A**) and 5A (**B**) during single-gas adsorption at 298 K. In the simulation, initially there are 100 C_2H_4 or C_2H_6 molecules in the gas reservoir of the supercell surface model before adsorption starts. Following the simulation, the molecules that enter the solid slab are counted as uptake. At 5 ns, the ideal selectivity (uptake ratio) of C_2H_4/C_2H_6 in zeolite ITQ-29 is 43.2, and that in zeolite 5A is 1.11.

The zeolite ITQ-29 exhibits higher ideal selectivity of C_2H_4/C_2H_6 (43.5 at 5 ns) than zeolite 5A (1.11). However, its sluggish growth in C_2H_4 uptake, especially in the internal region (Region 2, Figure S22) of the zeolite, as shown in Figure S23, suggests that zeolite ITQ-29 is not an excellent adsorbent for C_2H_4/C_2H_6 separation. Zeolite 5A exhibits a higher C_2H_4 uptake although its C_2H_4/C_2H_6 selectivity is low. Here, the ideal selectivity (1.11 at 298 K) is close to the value in reference (1.41 at 288 K) [52], which also validates the molecular dynamics simulations in this work. To improve the adsorption selectivity in zeolite 5A, the surface of the zeolite was modified with MPA to add a sieving layer that enables C_2H_4 molecules to preferentially permeate.

In mixture adsorption, the uptakes of C_2H_4 and C_2H_6 in zeolite 5A from equimolar binary mixture are shown in Figure 7. In the binary system, the C_2H_4 uptake is similar to that observed in single-gas adsorption, while the C_2H_6 uptake is inhibited due to competitive adsorption of C_2H_4. When the adsorption sites are occupied by C_2H_4 molecules which processes fast diffusion rate and strong affinity for the zeolite, it is difficult for C_2H_6 molecules to displace the adsorbed C_2H_4 molecules although there are still many C_2H_6 molecules in the gas reservoir, and therefore it results in lower C_2H_6 uptake. At 5 ns, the C_2H_4/C_2H_6 selectivity in the mixture adsorption increases to 2.72, whereas the ideal selectivity in single-gas adsorption is only 1.11, demonstrating the role of competitive adsorption in enhancing selectivity.

The uptakes of C_2H_4 and C_2H_6 in zeolite 5A for the 20:80 and 80:20 mixtures are shown in Figure S24. For a 20:80 mixture, 95% of C_2H_4 molecules are adsorbed in zeolite 5A (Figure S24A), whereas for an 80:20 mixture, only 23% of C_2H_6 molecules are adsorbed (Figure S24B). This indicates that C_2H_4 maintains its preferential adsorption over C_2H_6 across varying feed compositions.

In displacement adsorption, the uptakes of C_2H_4 and C_2H_6 in zeolite 5A are shown in Figure 8. When C_2H_6 molecules are pre-adsorbed in the zeolite, the C_2H_4 molecules in the gas reservoir rapidly enter the zeolite and displace the pre-adsorbed C_2H_6 molecules. At 6 ns, 63% of pre-adsorbed C_2H_6 molecules are displaced by C_2H_4 molecules, and then the system achieves dynamic equilibrium, as shown in Figure 8A. In reverse, when the C_2H_4 molecules are pre-adsorbed, the C_2H_6 uptake increases gradually and stabilizes at 38 molecules per supercell, as shown in Figure 8B, where the C_2H_6 molecules adsorb on

the vacant sites left after C_2H_4 adsorption while not displacing the pre-adsorbed C_2H_4 molecules. Moreover, there is no significant C_2H_4 desorption into the gas reservoir, indicating its stronger affinity for the zeolite as discussed in the adsorption energy calculations and mixture adsorption. The displacement adsorption phenomenon was also observed in experimental measurements [53,54].

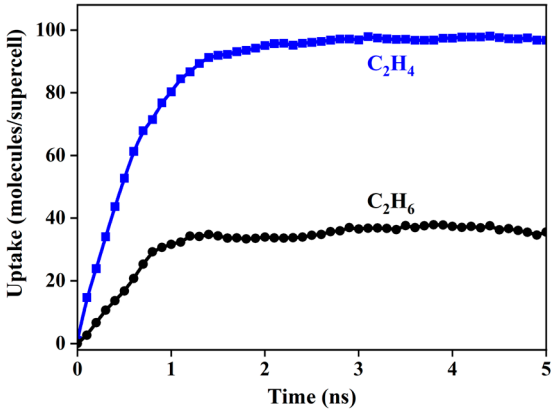


Figure 7. Uptakes of C_2H_4 and C_2H_6 in zeolite 5A during equimolar binary mixture adsorption at 298 K. In the simulation, initially there are 100 C_2H_4 and 100 C_2H_6 molecules in the reservoir of the supercell surface model before the adsorption starts. Following the simulation, the molecules that enter the solid slab are counted as uptake. At 5 ns, the C_2H_4/C_2H_6 adsorption selectivity in zeolite 5A is 2.72 for the equimolar binary mixture.

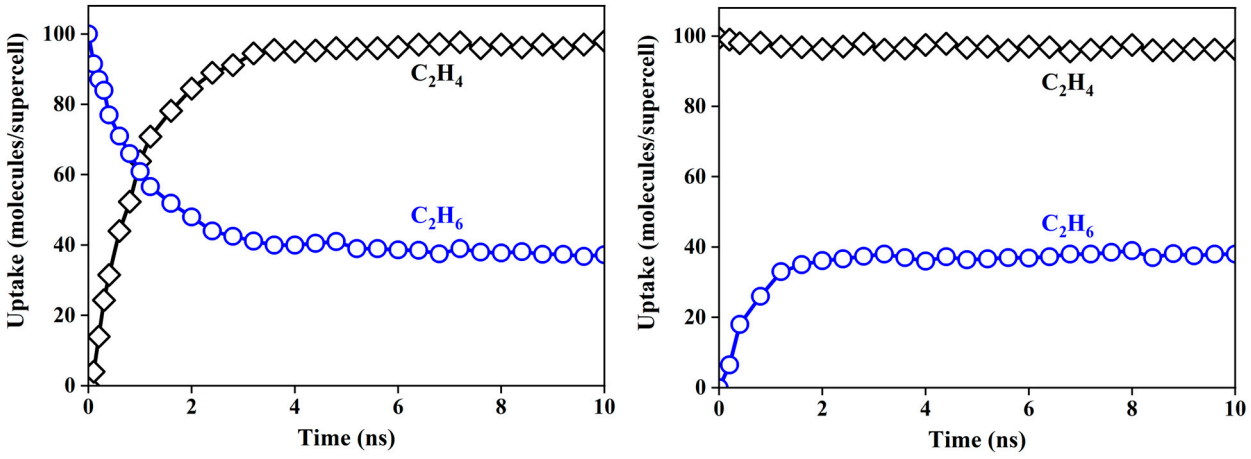


Figure 8. Uptakes of C_2H_4 and C_2H_6 in zeolite 5A during displacement adsorption at 298 K. In the simulation, initially there are 100 C_2H_6 molecules in the slab and 100 C_2H_4 molecules in the gas reservoir of the supercell surface model (**A**) or 100 C_2H_4 molecules in the slab and 100 C_2H_6 molecules in the gas reservoir (**B**) before the adsorption starts. Following the simulation, the molecules in the gas reservoir may displace the molecules pre-adsorbed in the solid slab.

3.5. Surface Modification

In single-gas adsorption, the uptakes of C_2H_4 and C_2H_6 in zeolite 5A with different coverages of MPA at 5 ns are shown in Figure 9, and the uptake kinetics curves are presented in Figure S25. With the increase in MPA coverage on the zeolite, the decrease magnitude of C_2H_6 uptake is larger than C_2H_4. At 25% coverage, the C_2H_4 uptake is nearly unaffected compared with the uncoated zeolite, while the C_2H_6 uptake decreases significantly. This indicates that the diffusion of C_2H_6 molecules passing through the MPA layer is strongly hindered due to the larger molecular size of C_2H_6 than C_2H_4. At 50% coverage, the C_2H_4

uptake remains nearly unaffected, while the C_2H_6 molecules are almost sterically excluded, where the MPA layer exhibits a sieving effect on the C_2H_6 molecules. At 75% coverage, C_2H_4 uptake is small and C_2H_6 uptake becomes undetectable. For efficient separation, the optimal MPA coverage on zeolite 5A is 50%, by which the ideal selectivity reaches 29.7 at 5 ns and the C_2H_4 uptake remains high. This demonstrates the efficacy of surface modification on the zeolites in tuning the separation of C_2H_4 and C_2H_6.

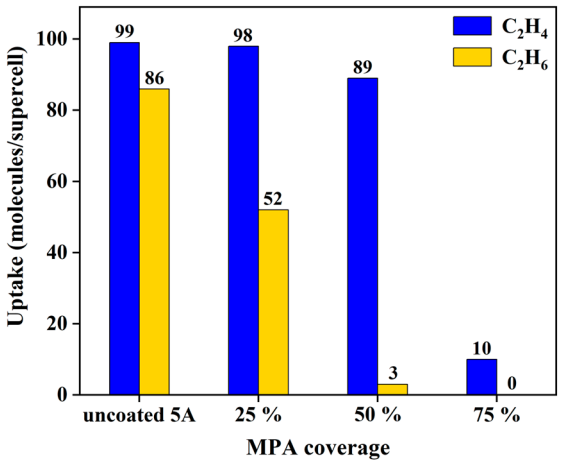


Figure 9. Uptakes of C_2H_4 and C_2H_6 in zeolite 5A with different coverages of MPA in single-gas adsorption at 5 ns and 298 K.

In equimolar binary mixture adsorption, the uptakes of C_2H_4 and C_2H_6 in zeolite 5A with 50% coverage of MPA are shown in Figure 10. In the binary system, the C_2H_4 uptake readily increases, similar to that in single-gas adsorption (Figure S25A), while the C_2H_6 uptake is low although there are many molecules in the gas reservoir. At 5 ns, the C_2H_4/C_2H_6 selectivity in mixture adsorption is 17.5. The C_2H_4 uptake in the central region of the zeolite increases rapidly with the progress of adsorption, as shown in Figure S26, indicating that the MPA coating tunes the diffusion of C_2H_4 molecules from the gas reservoir into the zeolite while not perturbing the molecular diffusion within the zeolite.

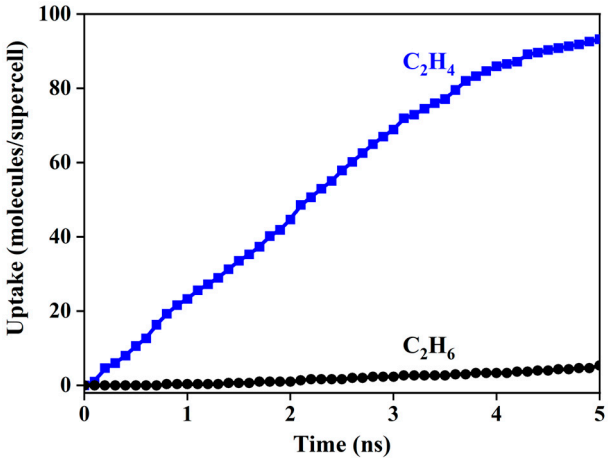


Figure 10. Uptakes of C_2H_4 and C_2H_6 in zeolite 5A with 50% coverage of MPA during equimolar binary mixture adsorption at 298 K. In the simulation, initially there are 100 C_2H_4 and 100 C_2H_6 molecules in the reservoir of the supercell surface model before the adsorption starts. At 5 ns, the C_2H_4/C_2H_6 adsorption selectivity in zeolite 5A with 50% coverage of MPA is 17.5 for the equimolar binary mixture.

In displacement adsorption, the uptakes of C_2H_4 and C_2H_6 in zeolite 5A with 50% coverage of MPA are shown in Figure 11. When C_2H_6 molecules are pre-adsorbed in the zeolite, the C_2H_4 molecules in the gas reservoir displace the pre-adsorbed C_2H_6 molecules progressively although the process is slow compared with that in uncoated zeolite 5A, in which the displacement has not completed even after 10 ns (Figure 11A). In reverse, when the C_2H_4 molecules are pre-adsorbed, the MPA coating effectively excludes the C_2H_6 molecules; the C_2H_4 uptake does not change throughout the simulation, demonstrating that the MPA coating prevents the C_2H_4 molecules from escaping the solid slab (Figure 11B). This indicates that the MPA coating tunes the molecular diffusion rate across the coating layer while preserving the competitiveness of C_2H_4 over C_2H_6 on the adsorption sites, enabling the small molecules to preferentially permeate [55].

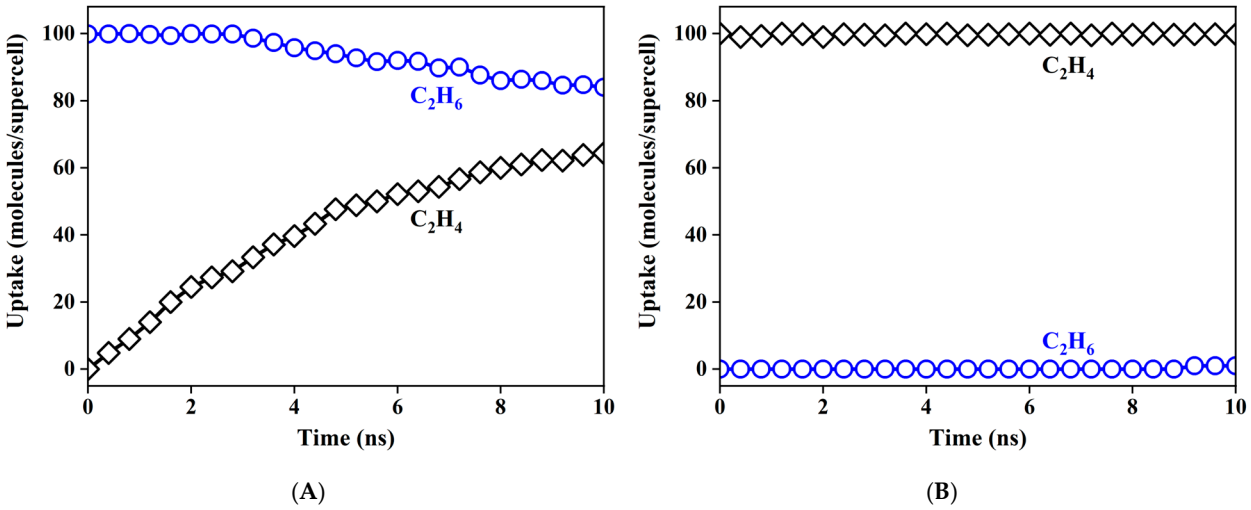


Figure 11. Uptakes of C_2H_4 and C_2H_6 in zeolite 5A with 50% coverage of MPA during displacement adsorption at 298 K. In the simulation, initially there are 100 C_2H_6 molecules in the slab and 100 C_2H_4 molecules in the gas reservoir (**A**) or 100 C_2H_4 molecules in the slab and 100 C_2H_6 molecules in the gas reservoir (**B**) before the adsorption starts.

4. Conclusions

According to the DFT calculations, the adsorption energies of gas molecules in zeolite 5A are more negative than in ITQ-29, and the difference in adsorption energy between C_2H_4 and C_2H_6 in zeolite 5A is significantly larger than that in ITQ-29, which is attributed to the exchangeable cations, facilitating strong interactions with C_2H_4 molecules through atomic orbital hybridization. According to the molecular dynamics simulations, zeolite ITQ-29 demonstrates high C_2H_4/C_2H_6 ideal selectivity (up to 43.5 at 5 ns) while exhibiting slow C_2H_4 uptake due to its small pore windows, which hinder C_2H_6 uptake but inadvertently suppress C_2H_4 uptake. Zeolite 5A facilitates faster diffusion of C_2H_4 molecules and exhibits a modest C_2H_4/C_2H_6 selectivity of 2.72 at 5 ns in binary mixture adsorption. MPA is introduced onto zeolite 5A to add a sieving layer that enables C_2H_4 molecules to preferentially permeate, by which it reduces the C_2H_6 uptake significantly while preserving the C_2H_4 uptake efficiency. The optimal coverage of MPA is 50%, yielding a C_2H_4/C_2H_6 selectivity of 17.5 at 5 ns in mixture adsorption. The displacement adsorption demonstrates that C_2H_4 possesses stronger affinity for the zeolite and readily displaces pre-adsorbed C_2H_6. These findings provide insights on designing high-performance adsorbents for the separation of olefins and alkanes.

Supplementary Materials: The following supporting information can be downloaded at: https://www.mdpi.com/article/10.3390/separations12060146/s1. Figure S1: oblique view of the struc-

tural model of zeolite 5A; Figure S2: adsorption isotherms of C_2H_4 at 298 K in zeolite 5A simulated with different atomic charges; Figure S3: top view (A) and front view (B) of the supercell surface model of zeolite ITQ-29; Figure S4: top view (A) and front view (B) of supercell surface model of uncoated zeolite 5A; Figure S5: top view (A) and front view (B) of supercell surface model of zeolite 5A fully coated with MPA; Figure S6: top view of 25% (A), 50% (B), 75% (C), and 100% (D) MPA-coated zeolite 5A; Figure S7: adsorption isotherms of C_2H_4 at 298 K in zeolite 5A simulated with different force fields; Figure S8: adsorption isotherms of C_2H_4 at 298 K in zeolite 5A simulated with different cutoff distances for van der Waals interactions; Figure S9: adsorption isotherms of C_2H_4 at 298 K in zeolite 5A simulated with different equilibrium steps; Figure S10: energy distribution profiles for C_2H_4 adsorption at 298 K in zeolite 5A simulated with different production steps; Figure S11: adsorption isotherms of C_2H_4 and C_2H_6 in zeolite ITQ-29 with CVFF forcefield at different temperatures; Figure S12: uptakes of C_2H_6 in zeolite 5A simulated at different temperatures; Figure S13: uptakes of C_2H_6 at 298 K in zeolite 5A simulated with different numbers of molecules in the gas reservoir; Figure S14: uptakes of C_2H_6 at 298 K in zeolite 5A simulated with different simulation timescales; Figure S15: uptakes of C_2H_6 at 298 K in zeolite 5A simulated with different supercell surface model thicknesses; Figure S16: partial density of states (PDOS) of the C atoms of C_2H_4 (A) and C_2H_6 (B) proximate to the 6-membered ring and the closest O atoms in host 6-membered ring of zeolite ITQ-29; Figure S17: partial density of states (PDOS) of the C atoms of C_2H_4 (A) and C_2H_6 (B) proximate to the 6-membered ring, the Ca atom near the 6-membered ring, and the closest O atoms in host 6-membered ring of zeolite 5A; Figure S18: adsorption isotherms for different C_2H_4/C_2H_6 mixtures (20:80, 40:60, 60:40, and 80:20) in zeolite ITQ-29 at 298 K; Figure S19: adsorption isotherms for different C_2H_4/C_2H_6 mixtures (20:80, 40:60, 60:40, and 80:20) in zeolite 5A at 298 K; Figure S20: energy distribution profiles for C_2H_4 and C_2H_6 adsorption in zeolites ITQ-29 (A) and 5A (B) under 101 kPa at 298 K; Figure S21: diffusion coefficients for C_2H_4 and C_2H_6 at 298 K in zeolite 5A with different loadings; Figure S22: schematic of the region division of the slab; Figure S23: C_2H_4 uptakes in different regions of zeolites ITQ-29 (A) and 5A (B) during single-gas adsorption at 298 K; Figure S24: uptakes of C_2H_4 and C_2H_6 for mixtures (20:80 and 80:20) in zeolite 5A at 298 K; Figure S25: C_2H_4 (A) and C_2H_6 (B) uptakes in zeolite 5A with different coverages of MPA during single-gas adsorption at 298 K; Figure S26: C_2H_4 uptakes at 298 K in different regions of zeolite 5A with 50% coverage of MPA; Figure S27: front view (A) and top view (B) of adsorption structure of C_2H_6 molecules in zeolite ITQ-29. Table S1: atomic coordinates of zeolite ITQ-29; Table S2: atomic coordinates of zeolite 5A; Table S3: average Hirshfeld atomic charges of adsorbents derived from DFT calculations; Table S4: electrostatic energies (kJ/mol) and loadings (molecules/α-cage) of C_2H_4 and C_2H_6 in zeolite 5A at 298 K and 100 kPa with different charges; Table S5: average Hirshfeld atomic charges of adsorbates derived from DFT calculations; Table S6: adsorption energies of C_2H_6 molecules in zeolite ITQ-29 with different loadings; Table S7: adsorption energies of light hydrocarbons in zeolite 5A at zero surface coverage; Table S8: adsorption parameters of the Langmuir model* for C_2H_4 adsorption in zeolite 5A; Table S9: diffusion coefficients (m^2/s) of C_2H_4 in zeolite 5A at different temperatures derived from simulations using different forcefields; Table S10: diffusion coefficients of C_2H_4 and C_2H_6 in zeolites ITQ-29 and 5A at different temperatures.

Author Contributions: Conceptualization, S.Z.; methodology, S.Z.; validation, M.A.E.; formal analysis, C.J.; investigation, X.Z.; data curation, X.Z.; writing—original draft preparation, X.Z.; writing—review and editing, S.Z., M.A.E., Z.C., Y.H., and G.W.M.; visualization, Z.C.; supervision, S.Z.; funding acquisition, S.Z. All authors have read and agreed to the published version of the manuscript.

Funding: This research was funded by National Natural Science Foundation of China (No. 22478229).

Data Availability Statement: The raw data supporting the conclusions of this article will be made available by the authors on request.

Conflicts of Interest: The authors declare no conflicts of interest.

Abbreviations

The following abbreviations are used in this manuscript:

DFT	Density functional theory
MD	Molecular dynamics
MPA	Methyl phosphonic acid
D	Diffusion coefficients

References

1. Almuqati, N.S.; Aldawsari, A.M.; Alharbi, K.N.; González-Cortés, S.; Alotibi, M.F.; Alzaidi, F.; Dilworth, J.R.; Edwards, P.P. Catalytic production of light olefins: Perspective and prospective. *Fuel* **2024**, *366*, 131270. [CrossRef]
2. Siracusa, V.; Blanco, I. Bio-polyethylene (Bio-PE), bio-polypropylene (Bio-PP) and bio-poly (ethylene terephthalate) (Bio-PET): Recent developments in bio-based polymers analogous to petroleum-derived ones for packaging and engineering applications. *Polymers* **2020**, *12*, 1641. [CrossRef] [PubMed]
3. Amghizar, I.; Vandewalle, L.A.; Van Geem, K.M.; Marin, G.B. New trends in olefin production. *Engineering* **2017**, *3*, 171–178. [CrossRef]
4. Zhao, Z.; Jiang, J.; Wang, F. An economic analysis of twenty light olefin production pathways. *J. Energy Chem.* **2021**, *56*, 193–202. [CrossRef]
5. Bereciartua, P.J.; Cantín, Á.; Corma, A.; Jordá, J.L.; Palomino, M.; Rey, F.; Valencia, S.; Corcoran, E.W., Jr.; Kortunov, P.; Ravikovitch, P.I.; et al. Control of zeolite framework flexibility and pore topology for separation of ethane and ethylene. *Science* **2017**, *358*, 1068–1071. [CrossRef] [PubMed]
6. Sholl, D.S.; Lively, R.P. Seven chemical separations to change the world. *Nature* **2016**, *532*, 435–437. [CrossRef]
7. Ren, T.; Patel, M.; Blok, K. Olefins from conventional and heavy feedstocks: Energy use in steam cracking and alternative processes. *Energy* **2006**, *31*, 425–451. [CrossRef]
8. Ruthven, D.M.; Reyes, S.C. Adsorptive separation of light olefins from paraffins. *Microporous Mesoporous Mater.* **2007**, *104*, 59–66. [CrossRef]
9. Mersmann, A.; Fill, B.; Hartmann, R.; Maurer, S. The potential of energy saving by gas-phase adsorption processes. *Chem. Eng. Technol.* **2000**, *23*, 937–944. [CrossRef]
10. Wang, B.; Li, Q.; Zhang, H.; Zhang, J.; Pan, Q.; Yan, W. Zeolites for the separation of ethylene, ethane, and ethyne. *Front. Chem. Sci. Eng.* **2024**, *18*, 108. [CrossRef]
11. Sun, Z.; Shu, Q.; Zhang, Q.; Li, S.; Zhu, G.; Wang, C.; Zhang, J.; Li, H.; Huang, Z. A hydrothermal synthesis process of ZSM-5 zeolite for VOCs adsorption using desilication solution. *Separations* **2024**, *11*, 39. [CrossRef]
12. Xing, J.; Jing, F.; Chu, W.; Sun, H.; Yu, L.; Zhang, H.; Luo, S. Improvement of adsorptive separation performance for C_2H_4/C_2H_6 mixture by CeO_2 promoted CuCl/activated carbon adsorbents. *Acta Phys.-Chim. Sin.* **2015**, *31*, 2158–2164. [CrossRef]
13. Sircai, S.; Golden, T.C.; Rao, M.B. Activated carbon for gas separation and storage. *Carbon* **1996**, *34*, 1–12. [CrossRef]
14. Cadiau, A.; Adil, K.; Bhatt, P.M.; Belmabkhout, Y.; Eddaoudi, M. A metal-organic framework-based splitter for separating propylene from propane. *Science* **2016**, *353*, 137–140. [CrossRef] [PubMed]
15. Zheng, S.; Xu, Y.; Yao, X.; Wang, C.; Liu, P.; Zhao, H.; Lu, J.; Ju, J. Efficient removal of tetracycline by metal-organic framework ZIF-67 and its mechanism. *Separations* **2024**, *11*, 63. [CrossRef]
16. Kan, X.; Wang, J.; Dong, Y. COFs as porous organic materials for the separation and purification of ethylene from C_2 hydrocarbons. *Chem. Commun.* **2024**, *60*, 13984–13997. [CrossRef] [PubMed]
17. Cao, X.; Zhang, Z.; He, Y.; Xue, W.; Huang, H.; Zhong, C. Machine-learning-aided computational study of covalent organic frameworks for reversed C_2H_6/C_2H_4 separation. *Ind. Eng. Chem. Res.* **2022**, *61*, 11116–11123. [CrossRef]
18. Zhang, X.; Li, L.; Wang, J.; Wen, H.; Krishna, R.; Wu, H.; Zhou, W.; Chen, Z.; Li, B.; Qin, G.; et al. Selective ethane/ethylene separation in a robust microporous hydrogen-bonded organic framework. *J. Am. Chem. Soc.* **2020**, *142*, 633–640. [CrossRef]
19. Zhang, X.; Wang, J.; Li, L.; Pei, J.; Krishna, R.; Wu, H.; Zhou, W.; Qin, G.; Chen, B.; Li, B. A rod-packing hydrogen-bonded organic framework with suitable pore confinement for benchmark ethane/ethylene separation. *Angew. Chem. Int. Ed.* **2021**, *60*, 10304–10310. [CrossRef]
20. Saha, D.; Kim, M.B.; Robinson, A.J.; Babarao, R.; Thallapally, P.K. Elucidating the mechanisms of paraffin-olefin separations using nanoporous adsorbents: An overview. *iScience* **2021**, *24*, 103042. [CrossRef]
21. Li, J.; Corma, A.; Yu, J. Synthesis of new zeolite structures. *Chem. Soc. Rev.* **2015**, *44*, 7112–7127. [CrossRef]
22. Feng, C.; E, J.; Han, W.; Deng, Y.; Zhang, B.; Zhao, X.; Han, D. Key technology and application analysis of zeolite adsorption for energy storage and heat-mass transfer process: A review. *Renew. Sustain. Energy Rev.* **2021**, *144*, 110954. [CrossRef]

23. Khaleque, A.; Alam, M.M.; Hoque, M.; Mondal, S.; Haider, J.B.; Xu, B.; Johir, M.A.H.; Karmakar, A.K.; Zhou, J.L.; Ahmed, M.B.; et al. Zeolite synthesis from low-cost materials and environmental applications: A review. *Environ. Adv.* **2020**, *2*, 100019. [CrossRef]
24. Treacy, M.M.J.; Foster, M.D. Packing sticky hard spheres into rigid zeolite framework. *Microporous Mesoporous Mater.* **2009**, *118*, 106–114. [CrossRef]
25. Padin, J.; Rege, S.U.; Yang, R.T.; Cheng, L.S. Molecular sieve sorbents for kinetic separation of propane/propylene. *Chem. Eng. Sci.* **2000**, *55*, 4525–4535. [CrossRef]
26. Liu, J.; Goss, J.; Calverley, T.; Liu, Y.; Broomall, C.; Kang, J.; Golombeski, R.; Anaya, D.; Moe, B.; Mabe, K.; et al. Carbon molecular sieve fiber with 3.4–4.9 angstrom effective micropores for propylene/propane and other gas separations. *Microporous Mesoporous Mater.* **2020**, *305*, 110341. [CrossRef]
27. Rege, S.U.; Padin, J.; Yang, R.T. Olefin/paraffin separations by adsorption: π-complexation vs. kinetic separation. *AIChE J.* **1998**, *44*, 799–809. [CrossRef]
28. Sala, A.; Pérez-Botella, E.; Jordá, J.L.; Cantin, A.; Rey, F.; Valencia, S. ITQ-69: A germanium-containing zeolite and its synthesis, structure determination, and adsorption properties. *Angew. Chem. Int. Ed.* **2021**, *60*, 11745–11750. [CrossRef]
29. Chen, H.; Wang, B.; Zhang, B.; Ren, Y.; Chen, J.; Gui, J.; Shi, X.; Yan, W.; Li, J.; Li, L. Enhancing the separation of C_2H_4/C_2H_6 in customized MOR zeolites. *Inorg. Chem. Front.* **2024**, *11*, 2427–2435. [CrossRef]
30. Baamran, K.; Moreno, J.D.L.; Rownaghi, A.A.; Rezaei, F. Kinetic assessment of light hydrocarbons separation over Fe-doped 13X composite sorbents under multicomponent feed conditions. *Ind. Eng. Chem. Res.* **2023**, *62*, 11917–11929. [CrossRef]
31. Ellis, L.D.; Parker, S.T.; Hu, J.; Zaccarine, S.F.; Stellato, M.J.; Funke, H.H.; Sievers, C.; Pylypenko, S.; Falconer, J.L.; Medlin, J.W. Tuning gas adsorption selectivity and diffusion rates in zeolites with phosphonic acid monolayers. *Cell Rep. Phys. Sci.* **2020**, *1*, 100036. [CrossRef]
32. Zhou, X.; Falconer, J.L.; Medlin, J.W. Organic-coated zeolites for selective gas adsorption: Effect of functional group identity and coating density. *Sep. Purif. Technol.* **2025**, *363*, 132040. [CrossRef]
33. Abdelrasoul, A.; Zhang, H.; Cheng, C.; Doan, H. Applications of molecular simulations for separation and adsorption in zeolites. *Microporous Mesoporous Mater.* **2017**, *242*, 294–348. [CrossRef]
34. Mitra, S.; Sharma, V.K.; Chaplot, S.L.; Mukhopadhyay, R. Diffusion of hydrocarbon in zeolite and effect due to pore topology: Neutron scattering and MD simulation studies. *Chem. Phys.* **2014**, *430*, 69–77. [CrossRef]
35. Guo, C.; Guan, Z.; Zhou, J.; Tang, S.; Zhang, C.; Zhao, K. Molecular insights into improved oxygen adsorption: Ag^+ and Ce^{3+} doping in Li-LSX for air separation. *Appl. Surf. Sci.* **2024**, *663*, 160186. [CrossRef]
36. Liu, S.; Lian, X.; Yue, B.; Xu, S.; Wu, G.; Chai, Y.; Zhang, Y.; Li, L. Control of zeolite local polarity toward efficient xenon/krypton separation. *J. Am. Chem. Soc.* **2024**, *146*, 8335–8342. [CrossRef]
37. Carey, T.; Corma, A.; Rey, F.; Tang, C.C.; Hriljac, J.A.; Anderson, P.A. The effect of extra framework species on the intrinsic negative thermal expansion property of zeolites with the LTA topology. *Chem. Commun.* **2012**, *48*, 5829–5831. [CrossRef]
38. Seff, K.; Shoemaker, D.P. The structures of zeolite sorption complexes. I. The structures of dehydrated zeolite 5A and its iodine sorption complex. *Acta Crystallogr.* **1967**, *22*, 162–170. [CrossRef]
39. Perdew, J.P.; Burke, K.; Ernzerhof, M. Generalized gradient approximation made simple. *Phys. Rev. Lett.* **1996**, *77*, 3865–3868. [CrossRef]
40. Seminario, J.M. Energetics using DFT: Comparions to precise ab initio and experiment. *Chem. Phys. Lett.* **1993**, *206*, 547–554. [CrossRef]
41. Ghosh, A.; Ma, L.; Gao, C. Zeolite molecular sieve 5A acts as a reinforcing filler, altering the morphological, mechanical, and thermal properties of chitosan. *J. Mater. Sci.* **2013**, *48*, 3926–3935. [CrossRef]
42. Ozturk, Z. Hydrogen storage on lithium modified silica based chabazite type zeolite, A computational study. *Int. J. Hydrogen Energy* **2018**, *43*, 22365–22376. [CrossRef]
43. Nam, G.M.; Jeong, B.M.; Kang, S.H.; Lee, B.K.; Choi, D.K. Equilibrium isotherms of CH_4, C_2H_6, C_2H_4, N_2, and H_2 on zeolite 5A using a static volumetric method. *J. Chem. Eng. Data* **2005**, *50*, 72–76. [CrossRef]
44. Gulianta, V.V.; Huth, A.J. Force fields for classical atomistic simulations of small gas molecules in silicalite-1 for energy-related gas separations at high temperatures. *J. Porous Mater.* **2013**, *20*, 741–751. [CrossRef]
45. Luca, G.D.; Pullumbi, P.; Barbieri, G.; Famà, A.D.; Bernardo, P.; Drioli, E. Gusev and Suter calculation of the diffusion coefficients of light gases in silicalite-1 membrane and silica-sodalite zeolite. *Sep. Purif. Technol.* **2004**, *36*, 215–228. [CrossRef]
46. Witte, N.D.; Robijins, S.; Denayer, J.F.M.; Dusselier, M.; Assche, T.R.C.V. Inverse gas chromatography study of n-alkane and 1-alkene adsorption on pure-silica LTA (ITQ-29) and CHA. *J. Phys. Chem. C* **2023**, *127*, 24393–24402. [CrossRef]
47. Derrah, R.I.; Loughlin, K.F.; Ruthven, D.M. Sorption of ethylene, propylene and cyclopropane in 5A zeolite. *J. Chem. Soc.* **1972**, *68*, 1947–1955. [CrossRef]
48. Bläker, C.; Mauer, V.; Pasel, C.; Dreisbach, F.; Bathen, D. Adsorption mechanisms of ethane, ethene and ethyne on calcium exchanged LTA and FAU zeolites. *Adsorption* **2024**, *30*, 1547–1564. [CrossRef]

49. Ghosal, P.S.; Gupta, A.K. Determination of thermodynamic parameters from Langmuir isotherm constant-revisited. *J. Mol. Liq.* **2017**, *225*, 137–146. [CrossRef]
50. Xu, Y.; Xu, J.; Yang, C. Molecule design of effective C_2H_4/C_2H_6 separation membranes: From 2D nanoporous graphene to 3D AHT zeolite. *J. Membr. Sci.* **2020**, *604*, 118033. [CrossRef]
51. Foster, M.D.; Rivin, I.; Treacy, M.M.J.; Delgado Friedrichs, O. A geometric solution to the largest-free-sphere problem in zeolite framework. *Microporous Mesoporous Mater.* **2006**, *90*, 32–38. [CrossRef]
52. Golipour, H.; Mokhtarani, B.; Mafi, M.; Moradi, A.; Godini, H.R. Experimental measurement for adsorption of ethylene and ethane gases on copper-exchanged zeolites 13X and 5A. *J. Chem. Eng. Data* **2020**, *65*, 3920–3932. [CrossRef]
53. Zhou, X.; Falconer, J.L.; Medlin, J.W. Competitive adsorption between propylene and propane on zeolite 5A and the influence of organic phosphonic acid coatings. *Sep. Purif. Technol.* **2024**, *346*, 127435. [CrossRef]
54. Li, X.; Yang, X.; Shang, H.; Liu, J.; Jin, X.; Wang, X.; Wang, Y.; Li, J.; Yang, J. Critical role of zeolite adsorbents in a displacement-adsorption separation process of methane-nitrogen gas. *Ind. Eng. Chem. Res.* **2025**, *64*, 2966–2976. [CrossRef]
55. Zhou, X.; Falconer, J.L.; Medlin, J.W. Mechanism of selectivity control for zeolites modified with organic monolayers. *Microporous Mesoporous Mater* **2022**, *337*, 111913. [CrossRef]

Disclaimer/Publisher's Note: The statements, opinions and data contained in all publications are solely those of the individual author(s) and contributor(s) and not of MDPI and/or the editor(s). MDPI and/or the editor(s) disclaim responsibility for any injury to people or property resulting from any ideas, methods, instructions or products referred to in the content.